Published in final edited form as:
Neuroscience. 2011 September 29; 192: 231–246. doi:10.1016/j.neuroscience.2011.06.016.

Calcium Currents of Olfactory Bulb Juxtaglomerular Cells: Profile and Multiple Conductance Plateau Potential Simulation

Arjun V. Masurkar[a,1] and **Wei R. Chen**[b]

[a]Department of Neurobiology, Yale University School of Medicine, New Haven, CT 06520

[b]Department of Neurobiology and Anatomy, University of Texas Medical School, Houston, TX 77030

Abstract

The olfactory glomerulus is the locus of information transfer between olfactory sensory neurons and output neurons of the olfactory bulb. Juxtaglomerular cells (JGCs) may influence intraglomerular processing by firing plateau potentials that support multiple spikes. It is unclear what inward currents mediate this firing pattern. In previous work, we characterized potassium currents of JGCs. We focus here on the inward currents using whole cell current clamp and voltage recording in a rat *in vitro* slice preparation, as well as computer simulation.

We first showed that sodium current was not required to mediate plateau potentials. Voltage clamp characterization of calcium current (I_{Ca}) determined that I_{Ca} consisted of a slow activating, rapidly inactivating ($\tau_{10\%–90\%\ rise}$ 6–8ms, $\tau_{inactivation}$ 38–77ms) component I_{cat1}, similar to T-type currents, and a sustained ($\tau_{inactivation} \gg 500$ms) component I_{cat2}, likely composed of L-type and P/Q-type currents. We used computer simulation to test their roles in plateau potential firing.

We robustly modeled I_{cat1} and I_{cat2} to Hodgkin-Huxley schemes (m^3h and m^2, respectively) and simulated a JGC plateau potential with 6 conductances: calcium currents as above, potassium currents from our prior study (A-type I_{kt1}, D-type I_{kt2}, delayed rectifier I_{kt3}), and a fast sodium current (I_{Na}). We demonstrated that I_{cat1} was required for mediating the plateau potential, unlike I_{Na} and I_{cat2}, and its $\tau_{inactivation}$ determined plateau duration. We also found that I_{kt1} dictated plateau potential shape more than I_{kt2} and I_{kt3}. The influence of these two transient and opposing conductances suggests a unique mechanism of plateau potential physiology.

Keywords

olfactory bulb; glomerulus; calcium current; potassium current; plateau potential; simulation

1. INTRODUCTION

Odor identity and concentration are represented by the combinatorial activation of distinct sets of glomeruli at the surface of the olfactory bulb (OB) (Stewart et al., 1979; Rubin and Katz, 1999; Mori et al., 1999; Johnson and Leon, 2000; Xu et al., 2003). Each glomerulus is

[1]Current Address/Correspondence to: Arjun V. Masurkar, Neurological Institute of New York, Columbia University Medical Center, 710 West 168th Street, 14th Floor, New York, NY 10032-3784, (P) 212-305-2343, (F) 212-305-2733, avm2114@columbia.edu.

a processing unit, receiving unique olfactory nerve input from olfactory sensory neuron (OSN) axons expressing the same olfactory receptor, which is then modulated by interactions with dendrites of interneurons and the projection neurons, mitral and tufted (M/T) cells (Ressler et al., 1994; Vassar et al., 1996; Mombaerts et al., 1996).

Juxtaglomerular cells (JGCs) are a heterogeneous group of neurons whose somata are near the border of an individual glomerulus, receiving input from OSNs and participating in complex synaptic interactions with other JGCs and M/T cells (Pinching and Powell, 1971a,b). JGCs are made up of interneurons such as periglomerular cells (PGCs) and short axon cells (SACs), as well as a subgroup of superficial tufted cell called external tufted cells (ETCs) (Pinching and Powell, 1971c; Shipley and Ennis, 1996).

In response to brief input, certain JGCs fire long lasting responses (Wellis and Scott, 1990; McQuiston and Katz, 2001; Hayar et al., 2004a; Zhou et al., 2006). One type of long lasting response is the spike burst, generated specifically by ETCs in a spontaneous and rhythmic fashion (McQuiston and Katz, 2001; Hayar et al., 2004a). In rat, ETC bursts are driven by persistent sodium current $I_{Na,P}$ (Hayar et al., 2004a), and in mouse by $I_{Na,P}$ and a low voltage activated (LVA) calcium current showing features of both T-type and L-type calcium current (Liu and Shipley, 2008). They also possess hyperpolarization-activated current (I_h) that may promote burst rhythmicity (Cadetti and Belluzzi, 2001; Liu and Shipley, 2008).

These ETC bursts may coordinate glomerular excitation through extensively branched primary dendrites giving numerous dendrodendritic synapses to other glomerular neurons (Pinching and Powell, 1971b; Pinching and Powell, 1971c; McQuiston and Katz, 2001; Hayar et al., 2004a; Zhou et al., 2006; Antal et al., 2006), as well as on physiological evidence that they can excite glomerular interneurons and mitral cells (Hayar et al., 2004b; Murphy et al., 2005; De Saint Jan et al., 2009) and engage in mutually electrical coupling (Hayar et al., 2005; Kosaka and Kosaka, 2005). In addition, inhibitory PGC activity prevents glomerular excitation by suppressing this critical ETC pathway (Gire and Schoppa, 2009).

Alternatively, some PGCs and ETCs fire plateau potentials spontaneously at low frequencies (McQuiston and Katz, 2001; Zhou et al., 2006). Despite extensive work on ETC burst mechanism and function, less is known regarding JGC plateau potential physiology. Input-output relationships in these neurons suggest that they can convert high frequency synaptic input into low frequency output (Zhou et al., 2006), but the network effect of this is unknown.

The mechanism of plateau potential firing is also less clear than the burst mechanism of ETCs. I_h may play a role in the excitability of PGCs and the rhythmic firing of JGC plateau potentials (Cadetti and Belluzzi, 2001; Zhou et al., 2006). Regarding the inward currents that create JGC plateau potentials, it is thought that they are low voltage-activated and not dependent on intracellular calcium (Zhou et al., 2006). Plateau potential persistence in extracellular TTX, sensitivity to 250μM extracellular nickel, and insensitivity to 200μM extracellular cadmium suggested a critical role for T-type calcium currents (Zhou et al., 2006; McQuiston and Katz, 2001). Such currents may be dendritically located (Zhou et al., 2006). This suggests that the plateau potential mechanism may be different than that of ETC bursts.

Low voltage activated (LVA) calcium current has been studied previously in other JGC subtypes. GABAergic PGCs in rat OB possess LVA calcium current, but it is blocked by dihydropyridines and cadmium and not by nickel, suggesting that these PGCs differ from plateau potential-firing PGCs (Murphy et al., 2005). Dopaminergic PGCs in mouse OB possess a T-type current, but it is blocked by 100μM nickel and 100μM cadmium (Pignatelli

et al., 2005). However, dopaminergic PGCs are not plateau potential-firing, and in this context T-type channels instead generates a subthreshold current that, along with $I_{Na,P}$, supports repetitive spiking in the absence of synaptic input (Puopolo et al., 2005). Therefore, it seems that plateau potential-firing neurons of the rat glomerulus possess a different LVA current to enable such prolonged depolarizations. This LVA current may be similar to that found in bursting mouse ETCs mentioned above, given that mouse ETC LVA current also promotes prolonged depolarizations and displays similar nickel sensitivity (Liu and Shipley, 2008).

In our accompanying study (Masurkar and Chen, 2011), we characterized the outward potassium currents of JGCs. Here, we pursued study of the calcium current of the JGCs with two purposes. First, we sought more specific evidence that JGCs possess a T-type calcium current that could mediate the plateau potential. Second, we created a single compartment computational model of plateau potential firing based on our characterizations. This enabled us to overcome pharmacological limitations and determine which inward currents (calcium, sodium) and potassium currents were critical for plateau potential generation.

2. EXPERIMENTAL PROCEDURES

2.1 Animal use and care

Animal experimentation protocols were reviewed and approved by the Yale University Animal Care and Use Committee. Sprague Dawley (*Rattus norvegicus*) rats, 12 to 21 days old, were anesthetized with 1.2g/kg urethane (intraperitoneal) until unresponsive to tail pinch and decapitated according to aforementioned committee guidelines. The number of animals used was minimized.

2.2 Slice preparation and solutions

Olfactory bulbs were extracted in chilled (4°C) and oxygenated (95% 0_2, 5% CO_2) artificial cerebrospinal fluid (ACSF), composed of 124mM NaCl, 2mM $CaCl_2$, 3mM KCl, 1.25mM NaH_2PO_4, 26mM $NaHCO_3$, 1.3mM $MgSO_4$, and 10mM dextrose at pH 7.4. Horizontal slices of 400μm thickness were made with a rotorslicer (Dosaka) and immediately immersed in oxygenated ACSF at 34°C for 15 to 20 minutes. Slices were maintained in oxygenated ACSF at room temperature for up to 8 hours.

For Na^+ washout experiments, slice preparation ACSF was made using a HEPES buffer (140mM NaCl, 3mM KCl, 1.3mM $MgSO_4$, 2mM $CaCl_2$, 10mM HEPES, 10mM dextrose). Oxygenation was achieved with 100% O_2.

Extracellular drugs (cadmium, nickel, mibefradil, TTX) were dissolved in ddH_20 except for nimodipine, which was dissolved in 100% EtOH such that final ethanol concentration was 0.02%. These stock solutions were stored in refrigeration, except for TTX, which was stored at −20°C.

2.3 Current clamp recording

JGCs were recorded in whole cell mode using a Kgluconate-EGTA internal solution (130mM Kgluconate, 10mM HEPES, 0.2mM EGTA, 4mM MgATP, 0.3mM Na_3GTP, and 10mM Na_2phosphocreatine), adjusted to pH 7.3–7.4 with KOH.

JGCs were visually identified via an infrared camera (Hamamatsu C2400-07ER) on an upright microscope (Olympus BX50WI) employing differential interference contrast microscopy with a 40X water immersion objective. JGCs were identifiable by their large somata at the deep border of glomeruli. Based on their size, we felt that these cells were

similar to the external tufted cells and larger periglomerular cells that have been morphologically identified and shown to exhibit plateau potentials (McQuiston and Katz, 2001; Zhou et al., 2006). In unpublished work, we have also demonstrated that some of these cells give glutamatergic output, and are therefore most likely external tufted cells (results not shown). Current clamp whole cell recordings were made with the Axoclamp 2A and 2B amplifiers in bridge balance current clamp mode. Data were acquired with Pclamp 9.0 software at 10–20kHz sampling rate. Pipettes of resistance 8–12MΩ were pulled from borosilicate glass tube with filament (1.20mm outer/0.69mm inner diameter; Sutter) using a P-97 Flaming/Brown micropipette puller (Sutter). The recording chamber contained ACSF heated to 33–37°C.

For Na^+ washout experiments, HEPES-buffer control ACSF was replaced with an ACSF in which Na^+ was replaced with equimolar Tris (140mM TrisCl, 3mM KCl, 1.3mM $MgSO_4$, 2mM $CaCl_2$, 10mM HEPES, and 10mM dextrose).

2.4 Voltage clamp recording

For voltage clamp characterization of calcium current, the following intracellular solution was used: 100mM CsMES, 10mM TEA-Cl, 10mM EGTA, 0.5mM $CaCl_2$, 10mM HEPES, 5mM MgATP, 10mM Na_2phosphocreatine, and 0.5mM Na_3GTP at pH 7.4 (CsMES internal solution). The EGTA and $CaCl_2$ clamped internal calcium concentration to a known level of approximately 80nM, resulting in a theoretical Ca^{2+} reversal potential of +134mV. However, due to nonlinear properties of lipid membrane (Goldman, 1943; Hodgkin and Katz, 1949), the apparent reversal potential by linear extrapolation of IV curves was much less (+35mV).

The following were added to ACSF for further calcium current isolation: 1 μM TTX to block fast Na^+ current, 3mM CsCl to block hyperpolarization-activated current (I_h), 50μM D-APV to block NMDAR-mediated glutamatergic input, and 20μM CNQX to block AMPAR-mediated glutamatergic input. Calcium replacement with barium (Hagiwara et al., 1975) was not done in order to study the native kinetics and amplitudes of calcium currents in the JGC.

Pipettes were pulled as above to 3–5MΩ (initial series resistance below 20MΩ) and tips were coated with dental wax to reduce capacitance. An axoclamp 200B amplifier was used for recordings in whole cell voltage clamp cSEVC mode.

JGCs were first identified by morphology as above. Plateau potential firing was confirmed before dialysis with K^+ channel blocking internal solution by testing responses to olfactory nerve (ON) input in extracellular gigaseal mode just prior to break-in. The ON layer was preserved in the coronal acute slices, and its stimulation was elicited by placing a large tip pipette (1MΩ) filled with ACSF or a concentric bipolar stimulating electrode (25μm diameter tip) that was connected to electrical isolator, which controlled current amplitude of stimulation. Nerve was stimulated with one shock of 0.05–0.2ms width and less than 0.1mA amplitude.

After JGC identification, pipette capacitance was compensated and membrane was ruptured. The cell was dialyzed at resting membrane potential for several minutes. Series resistance (R_s), along with membrane capacitance (C_m), was compensated (with 10μs lag) to at least 80% correction and prediction for kinetics and activation/inactivation experiments and at least 65% for pharmacology experiments. If uncompensated R_s exceeded 20MΩ the recording was discontinued.

Currents were P/4 leak subtracted online. Data were sampled and filtered at 2 or 5kHz based on presumed Nyquist rate dependent on low pass filtering by the series resistance at $1/2\pi R_s C_m$ (with uncompensated R_s usually much less than 20MΩ, this cutoff frequency was typically much higher than ~250Hz). When possible, protocols were repeated and averaged. All voltages were corrected for a liquid junction potential of 10mV between ACSF and CsMES internal solution, measured according to a KCl salt bridge-based method (Neher, 1992). All experiments were performed at 33–37°C.

2.5 Computer simulation

Currents were assumed to be generated by homogeneous conductances undergoing state transitions according to a Hodgkin-Huxley scheme for activation (m) and inactivation (h) (Hodgkin and Huxley, 1952):

$$m(V_m, t)=m_\infty (1 - e^{t/\tau m}), \quad [1]$$

where

$$m_\infty(V_m)=\tau_m(V_m)/(\tau_m(V_m)+\tau_m(V_m)) \quad [2]$$

$$\tau_m=1/(\tau_m(V_m)+\tau_m(V_m)) \quad [3]$$

for activation (m) and analogous equations for inactivation (h). Current amplitude was determined by the following:

$$I=G * m^X(V_m, t) * h^Y(V_m, t) * (V_m-E_{rev}) \quad [4]$$

We determined experimental values to simulate these equations based on modifications of prior methods (Connor and Stevens, 1971c; Huguenard and McCormick, 1992). Briefly, during voltage clamp experiments, $m_\infty^X(V_m)$ was assumed to be equivalent to $G/G_{max}(V_m)$ obtained by the steady state activation protocol. This involved measuring peak current (I_{peak}) generated at different test potentials from a given holding potential. This holding potential was chosen where current was maximally recovered from inactivation, and required the assumption that activation occurred much faster than inactivation to establish peak current. This held true in the case of the transient currents. Conductance value was determined by the following and normalized for each cell by dividing my the maximal conductance:

$$G=I_{peak}/(V_{test}-E_{rev}) \quad [5]$$

The value of X was determined for each transient current by fitting Boltzmann functions of the appropriate power to $G/G_{max}(V_m)$ and then examining how well macroscopic current generated in NEURON simulations fit experimentally recorded traces (see below and Results). Similarly, $h_\infty(V_m)$ was assumed to be equivalent to I/I_{max}, derived from the steady state inactivation protocol which generated I/I_{max} for a given test potential as a function of holding potential. Test potential had been chosen to maximize activation and isolation of the current of interest. We assumed Y = 1, as in most conductance models.

The time constants, $\tau_m(V_m)$ and $\tau_h(V_m)$ could be constructed by measuring the rate of activation/deactivation and inactivation/recovery from inactivation, respectively. Time constant of activation was determined from the 10%–90% rise time of currents elicited in the activation protocol as follows. Because different schemes were used (X=1,2,3…), converting the rise time (t_{rise}) to a time constant required different conversion factors for each value of X, derived by solving for t_{rise} = t90–t10 in the following system of equations:

$$0.9\, I_{max} = I_{max}\,(1 - e^{-t90/tm})^X \quad [6]$$

$$0.1\, I_{max} = I_{max}\,(1 - e^{-t10/tm})^X \quad [7]$$

This lead to a scaling factor as follows:

$$\tau_m = t_{rise}/(\ln((1-(0.1)^{1/X})/(1-(0.9)^{1/X}))) \quad [8]$$

Time constant of deactivation was determined by monoexponential fits to decay current elicited by stepping voltage to hyperpolarized potentials after current activation to a given test potential. The function $\tau_m(Vm)$ was constructed by combining these two functions. We assumed that the closing of a channel needed only one of the X number of m gates to deactivate, and therefore each time constant was scaled by 1/X based on the scheme being tested (Huguenard and McCormick, 1992). Time constant of inactivation was determined from monoexponential fits to decay of currents elicited in the activation protocol. Time constant of recovery from inactivation was determined by monoexponential fits to recovery of current after different durations of a hyperpolarized holding potential. The function $\tau_h(Vm)$ was constructed by combining these two functions.

The NEURON simulation environment version 5.9 (Hines and Carnevale, 1997) was used to simulate currents and a single compartment neuron containing these currents. The morphological parameters of the cell were chosen to match capacitative transients produced in these cells in current clamp, as well as capacitance in ranges seen in voltage clamp. These and the passive parameters are shown in Table 3. Currents were modeled using equations fit to $m_\infty{}^X(V_m)$, $h_\infty{}^Y(V_m)$, $\tau_m(V_m)$, and $\tau_h(V_m)$ wherever possible, and incorporated in NMODL. For simulations generated completely *de novo* (I_{cat1}, I_{kt1}, I_{kt2}), the following differential equation was used in NEURON to actively compute m(Vm,t), and analogously for $h(V_m,t)$:

$$m' = (m_\infty(Vm) - m(Vm,t))/\tau_m \quad [9]$$

For I_{cat2}, I_{kt3}, and I_{Na}, we based simulations on code used in previously published models (Traub et al., 2003; Mainen et al., 1995; Shen et al., 1999, respectively). Simulation runs were computed with time step of 0.025ms.

2.6 Statistical Analysis

Numerical averages are presented with standard error values, unless otherwise noted. P-values were obtained by Welch's unpaired T-test. Correlations were evaluated using Pearson coefficient (r values presented).

3. RESULTS

3.1 The role of sodium current in JGC plateau potential generation

Though previous studies have shown that JGC plateau potentials are not blocked by extracellular TTX (McQuiston and Katz, 2001; Zhou et al., 2006), ruling out classical fast and persistent Na^+ conductances as mediators of the firing pattern, there existed the possibility that TTX-resistant sodium currents could play a role (Yoshida and Matsuda, 1979). This was addressed in one study (McQuiston and Katz, 2001), in which plateau potentials persisted when extracellular Na^+ was replaced with choline, and when the cell was dialyzed with QX-314, a lidocaine derivative Na^+ channel blocker. However, neurons have variable permeability to choline (Partridge et al., 1994). Furthermore, QX-314 is known to also block calcium current (Talbot and Sayer, 1996).

We therefore aimed to block all Na^+ currents by replacing extracellular sodium with impermeable $Tris^+$ base (see Methods). Figure 1A shows a typical plateau potential, elicited in whole cell mode via a small current injection, before and after sodium replacement (n = 8). We waited well after the preliminary action potential was eliminated to consider sodium to be effectively washed out. Indeed, the underlying depolarization of the plateau potential persisted with Na^+ gradient eliminated. We calculated the area of the plateau potential, measured as the product of half-maximal amplitude ($V_{max,1/2}$) and plateau duration at $V_{max,1/2}$, before and after experimental manipulation. Figure 1B shows that the area of the plateau potential, as a percent of area before Na^+ replacement, is only slightly reduced (77.9 +/− 16.5%). For comparison, in another set of cells, we made this measurement before and after addition of TTX (n = 10). As a percent of control, plateau potential area on average was similar after TTX (109.5% +/− 61.5%).

3.2 Calcium current in JGCs: fast (I_{cat1}) and slow (I_{cat2}) components

With evidence in our prior study eliminating calcium-mediated processes as generators of plateau potentials (Zhou et al., 2006), and with evidence above against a critical role for Na^+ current, the most likely candidate to mediate the plateau potential seemed to be voltage dependent calcium currents (VGCCs). Previous work established that the plateau potential was sensitive to 250μM to 1mM extracellular nickel but not 200 to 400μM extracellular cadmium (McQuiston and Katz, 2001; Zhou et al., 2006). Though this supported that T-type calcium currents were driving the plateau potential, at such elevated (>100μM) concentrations, multiple subtypes of calcium current were likely blocked by either cation (Fox et al., 1987; Zamponi et al., 1996). Mibefradil, a T-type calcium channel blocker of debatable specificity (Avery and Johnston, 1997; Randall and Tsien, 1997), also produced inconclusive results for the same reasons (data not shown).

Due to this limitation of pharmacology, we turned to voltage clamp characterization. We isolated the calcium current (I_{Ca}) as described in the Methods. I_{Ca} was evoked by 5mV step depolarizations from an adequately hyperpolarized holding potential, chosen to relieve most currents from inactivation (V_{hold} = −90mV). Figure 2A shows typical currents generated from this protocol (n = 14). I_{Ca} had two components (Figure 2B): one transient (I_{cat1}), one more sustained (I_{cat2}). I_{cat1} decayed with time constants much less than 100ms, and we measured its amplitude as the difference of between the I_{Ca} peak and the sustained current I_{Ca2} at 200ms. I_{cat2} often had decay time constants well exceeding 500ms.

We were able to obtain stable, consistent recordings of each component for up to 31 minutes (Figure 2C, n = 12). Figure 2D shows a plot of the maximum current amplitudes of each component for all recorded cells (n = 27). The ratios of the two components varied widely, with I_{cat2}/I_{cat1} ranging from 0.52–3.12 and with correlation coefficient (Pearson r) of 0.57. Therefore, it seemed more likely that I_{Ca} was generated by at least two different populations

of voltage dependent current, rather than one current with two kinetic components, as is found with N-type current (Plummer and Hess, 1991). This was further supported by the average current-voltage relation (IV curve), as in Figure 2E (n = 8). Resting membrane potential (V_{rest}), action potential threshold ($V_{APthresh}$), and plateau voltage range ($V_{plateau}$) are delineated on the graph based on values obtained in the accompanying potassium current study (Masurkar and Chen, 2011). Note that the IV curve of I_{cat1} reaches its peak at lower voltages than I_{cat2} and that it is higher in amplitude between V_{rest} and $V_{plateau}$. However, both currents possessed activation thresholds near the resting membrane potential of these JGCs.

To gather more evidence that these were distinct currents, we attempted to separate the two components by assessing the effect of holding potential on peak amplitude. We repeated IV curves at two different holding potentials, one high (−60mV) and one low (−90mV). I_{cat1} had peak activation at −30mV, as in Figure 2E. However, I_{cat1} elicited from −60mV was lower in amplitude than that elicited from −90mV (Figure 3Ai). A similar comparison with a test potential of −15mV, at which I_{cat2} peaked, demonstrated that this sustained current was not as affected by manipulation of holding potential (Figure 3Aii). The influence of holding potential was quantified across a range of test potentials in Figures 3B and 3C, showing the average normalized IV curves for I_{cat1} and I_{cat2}, respectively (n = 8). This again confirmed the distinctness of these two components. Furthermore, the voltage dependence of I_{cat1} resembled the voltage dependence of the plateau potential in the presence of TTX, as demonstrated in our prior work (Zhou et al., 2006).

To be able to test the role of each current in plateau potentials, we tried to separate the two currents by using combinations of nickel, cadmium, nimodipine, and mibefradil. However, this was unsuccessful in that recordings were often unstable and results obtained were again nonspecific (data not shown).

3.3 Further characterization of I_{cat1}

To overcome this pharmacological limitation, our strategy for assessing the function of I_{cat1} was to fully characterize the voltage dependence and kinetics to permit simulation and development of a model for plateau potential generation in which I_{cat1} could be selectively removed and altered *in silico*.

To study steady state inactivation of this current, we varied V_{hold} from −45mV to −110mV. We used a test pulse (V_{test}) to −40mV so I_{cat1} would be activated but minimally contaminated by I_{cat2}. Shown in Figure 4A are currents generated by this inactivation protocol, demonstrating reduced I_{cat1} at depolarized holding potentials (n = 7). Figure 4Bi shows an overlay of the normalized I_{cat1} for each V_{hold} in a given inactivation protocol. The similarity between each normalized trace within the protocol demonstrated that the currents generated in this voltage range are likely from a uniform population of voltage activated currents. We quantify this in Figure 4Bii, showing that the time constant of inactivation ($\tau_{inactivation}$) is on average consistent at each V_{hold} (n = 7). The values for $\tau_{inactivation}$ were obtained by a fitting the decay of I_{cat1} to monoexponential decay.

Steady state inactivation, as a function of V_{hold}, was determined by dividing current amplitudes by the maximum elicited within a protocol (I/I_{max}). Figure 4C demonstrates that I_{cat1} smoothly inactivated with voltage (n = 7). This also reveals that I_{cat1} is approximately 90% inactivated at V_{rest}. Shown with the steady state inactivation curve is the steady state activation curve. IV curve of I_{cat1} from figure 2D was converted into an activation curve by dividing current by the driving force, and normalizing this conductance (G) by the maximum (G_{max}) for each protocol per neuron (n = 14). This confirmed that I_{cat1} displayed smooth activation with voltage, typical of uniform voltage gated currents.

To measure kinetics of activation and inactivation, we analyzed currents from the IV curve of Figure 2. Delineated in Figure 5Ai is the method by which these were measured. Briefly, time to peak was measured by assessing the time needed to rise from 10% of maximum to 90% of maximum. For inactivation rate, $\tau_{inactivation}$ was obtained as described above. Shown in Figures 5Aii and 5Aiii are plots delineating how $t_{10\%–90\%max}$ (n = 5) and $\tau_{inactivation}$ (n = 5) smoothly vary with voltage, respectively. Notable was that $\tau_{inactivation}$ resembled the duration of the plateau potential.

The time constant of recovery from inactivation (or $\tau_{recovery\ from\ inactivation}$) was measured as function of V_{hold} as follows. I_{cat1} was evoked by a V_{test} from a negative V_{hold}, fully inactivated, exposed to a recovery potential ($V_{recovery}$) for different durations, and evoked again at the same V_{test} (Figure 5Bi). I_{cat1} amplitude recovery with time was fit to a monoexponential to obtain $\tau_{recovery\ from\ inactivation}$. We tested $\tau_{recovery\ from\ inactivation}$ at two values for $V_{recovery}$: −30mV and −40mV. Shown in Figure 5Bii is a plot of how $\tau_{recovery\ from\ inactivation}$ varied with recovery potential (n = 4–5 for each recovery potential). Interestingly, the time course of recovery from inactivation for I_{cat1} was in the same range as the frequencies of rhythmic plateau potential generation.

Time constant of deactivation ($\tau_{deactivation}$), as a function of V_m, was measured by eliciting I_{cat1} with brief V_{test} to −30mV, and then rapidly stepping to various potentials once I_{cat1} reached its peak (Figure 5Ci). The resulting tail current decays were fit to monoexponentials to obtain $\tau_{deactivation}$. Shown in Figure 5Cii is a graph of how $\tau_{deactivation}$ smoothly varied with voltage (n = 5).

3.4 Simulation of calcium currents

To simulate the calcium currents of JGCs, we approximated the total I_{Ca} as a sum of I_{cat1} and I_{cat2}. We simulated I_{cat2} by modifying an existing model for L-type conductance, which used an m^2 Hodgkin-Huxley scheme, without inactivation (Traub et al., 2003). Shown in Figure 6A is a fit of the simulation activation curve to our experimental data. The experimental activation curve was generated from the activation protocol similar to the method used for I_{cat1}. Figure 6B shows the kinetics of activation for the simulation. Equations for this model are in Table 1.

To simulate I_{cat1} we employed our extensive characterization of steady state activation, inactivation, and kinetics. Because models for transient VGCCs, the T-type currents, have used mh, m^2h, and m^3h schemes (De Schutter and Bower, 1994; Jaffe et al., 1994; Huguenard and McCormick, 1992; Lee et al., 2003; Wang et al., 1991a), we tested all three for fitness. Shown in Figure 6C are three Boltzmann curves which, when raised to the power of n = 1 or 2 or 3, robustly overlapped the experimental activation curve m_∞ curve. Shown in Figure 6D is the Boltzmann curve fit to the steady state inactivation plot (h_∞ curve).

For kinetics, we simulated τ_m by a function fit to the combination of $\tau_{deactivation}$ and $\tau_{activation}$. For the latter, for each model scheme (mh, m^2h, and m^3h), we converted experimental $t_{10\%-90\%max}$ to an appropriately scaled exponential time constant $\tau_{activation}$ according to the number of m components (see Methods). This led to three different τ_m functions. The converted data and fits for each model are shown in Figure 6E. For τ_h, we fit functions to the grouping of $t_{inactivation}$ with $t_{recovery\ from\ inactivation}$, as shown in Figure 6F. Because all three models had one inactivation particle, the same τ_h function was used for all three. These fits generated $m(V_m,t)$ and $h(V_m,t)$ to complete each simulation. For each scheme, in simulated voltage clamp, we generated currents at one subthreshold (V_{test} = −55mV) and one suprathreshold (V_{test} = −30mV) test potential to test which model fit best to an average of experimental traces for the same test potentials. As shown in Figure 6Gi

and Figure 6Gii, the m^3h current best fit the experimental traces. Equations for this model are in Tables 1 and 2.

3.5 Single compartment modeling of JGC plateau potential firing

We combined our simulations of calcium current with those for the three potassium currents (I_{kt1}, I_{kt2}, I_{kt3}) in the accompanying study (Masurkar and Chen, 2011), and a previously published fast sodium current I_{Na} (Shen et al., 1999), to generate a single compartment model of plateau potential firing in JGCs (equations in Tables 1 and 2). I_{kt1} is an A-type current, I_{kt2} is a D-type current, and I_{kt3} is a delayed rectifier. We used passive properties to be consistent with range of whole cell capacitance (C_m) and resistances (R_m) in our voltage clamp recordings, modulated to recreate capacitative transients recorded in current clamp (Table 3). Conductance values of each calcium and potassium current were based on ranges noted in voltage clamp recordings, normalized by cell capacitance. Ratios of I_{cat2}:I_{cat1} and I_{kt3}:I_{kt2}:I_{Kkt1} were also noted in our recordings and used to guide conductance density choices. We modulated these values, as well as that of the sodium current, to align reasonably with standardized recordings of plateau potentials. Calcium-activated potassium currents were not included, as we have previously shown these currents play minimal roles in shaping the salient features of the plateau potential (Zhou et al., 2006; Masurkar and Chen, 2011).

The summary of the model is shown in Figure 7A, demonstrating all m_∞ and h_∞ curves for the 6 conductances of the simulation, and Table 3, which shows parameters for conductance values and passive characteristics. An example of a simulated plateau potential at resting membrane potential (V_{rest} = −63mV) is shown in Figure 7B. Below is shown the time course of each ion current used in the model. The model demonstrated similar electrical properties to experimental recordings. For example, repetetive firing of plateau potentials is limited to certain frequencies (Zhou et al., 2006). Our simulation also showed this property. Robust plateau potentials could be induced by current input every 240ms (Figure 7C, above), but when inputs were delivered every 130ms there was variation in plateau duration (Figure 7C, below). Note that 240ms is three times $\tau_{\text{recovery from inactivation}}$ for I_{cat1} at this V_{rest}.

We then used the simulation to explore the roles of inward currents in plateau potential generation. In Figure 8A, we show that a significant afterdepolarization persists in the absence of sodium current, as we have found experimentally. This shows that I_{cat1} and I_{cat2} both support the plateau potential under these conditions. In Figure 8B, we selectively removed I_{cat1} to demonstrate that I_{cat2} and I_{Na} cannot support the plateau potential. In Figure 8C, we selectively remove I_{cat2} to show that I_{cat1} together with I_{Na} can generate the plateau potential. These simulations indicate that I_{cat1} is necessary, though not necessarily sufficient, for generating the plateau potential. In Figure 8C we removed only I_{cat2} to demonstrate that a depolarizing potential persists, driven by I_{cat1} and I_{Na}. In the same figure, removal of both I_{Na} and I_{cat2} reduced, but did not eliminate, the depolarizing potential mediated by I_{cat1} alone.

We exploited the ability to manipulate I_{cat1} to further explore which aspects of the current were critical for plateau potential timing. Since the plateau potential level is at approximately −30 mV, where the activation and inactivation processes of I_{cat1} are dominant over deactivation and recovery from inactivation, we sought to manipulate these values and test their effect on the plateau potential. Figure 8D demonstrates a plateau potential generated with alternate forms of I_{cat1} in which $\tau_{\text{activation}}$ was increased and decreased by a factor of two. This manipulation caused slight variation in plateau duration. In Figure 8E, we show the plateau potential generated with $\tau_{\text{inactivation}}$ increased and

decreased by a factor of two showed much more variation. Therefore, the inactivation kinetics of I_{cat1} greatly influence plateau potential shape.

We then explored the role of potassium currents. For each potassium current we increased and decreased conductance by 25%. In Figure 9A is shown the effects of such modulations of $I_{kt1.}$ This demonstrated that this atypical A-current had a wide influence over the potential, including spike amplitude, spike delay, plateau amplitude, and plateau duration. In Figures 9B and 9C we similarly altered the conductance values of I_{kt2} and I_{kt3}. These manipulations did not have much effect.

4. DISCUSSION

In this study we first demonstrated that JGC plateau potentials are primarily mediated by voltage gated calcium currents and not by sodium influx. We then characterized the two components of JGC calcium current: a slow activating, rapidly inactivating ($\tau_{10\%–90\%\ rise}$ 6–8ms, $\tau_{inactivation}$ 38–77ms) component I_{cat1} and a sustained ($\tau_{inactivation} \gg 500$ms) component I_{cat2}. To overcome limitations of pharmacological separation, we created a 6-conductance computer model of JGC plateau potentials to then demonstrate that I_{cat1} was the most critical inward current for plateau potential generation and that I_{kt1}, an A-type potassium current, was the most important outward current for plateau potential shape.

$I_{Na,P}$ influences burst and plateau potential firing in several neuronal subtypes (Kay et al., 1998; Hsiao et al., 1998; Jahnsen and Llinas 1984a; Jahnsen and Llinas 1984b; Li and Bennett, 2003), including OB ETCs (Hayar et al., 2004a; Liu and Shipley, 2008). Prior studies showed that this current does not mediate the JGC plateau potential (McQuiston and Katz, 2001; Zhou et al., 2006), and in the present study we used another pharmacologic manipulation to suppress Na^+ current ($Tris^+$ replacement) and demonstrate that this did not abolish the plateau potential either. Nevertheless, fast Na^+ currents are likely still critical as a trigger, because an action potential is probably needed to activate the other inward currents involved plateau potential generation. The mild reduction in plateau potential area by our manipulation implied that sodium ions also contributed to plateau amplitude and duration. This could come in the form of TTX-resistant Na^+ currents, nonspecific cation currents, or current from Na^+-Ca^{2+} exchangers.

I_{cat1} likely represents a uniform population of currents based on the smoothly voltage-dependent activation, inactivation, and kinetics. Additionally, we demonstrated that $\tau_{inactivation}$ was stable over a wide range of holding potentials. Rapidly inactivating VGCCs include T-type, R-type, and N-type currents. Immunohistochemical evidence exists for all of these calcium subtypes in the glomerular layer (Ludwig et al., 1997; Talley et al., 1999).

The half maximal voltage ($V_{1/2}$) for inactivation was −74.0mV, which is similar to that of typical whole cell T-current and T-type channels (Coulter et al., 1989; Monteil et al., 2000a; Monteil et al., 2000b; Klockner et al., 1999), R-current (Soong et al., 1993; Randall and Tsien, 1997), and N-current (Stea et al., 1999). However, the activation $V_{1/2}$ of I_{cat1} is −40.5mV, approximately 10mV hyperpolarized to that of the R-current (Soong et al., 1993; Randall and Tsien, 1997) and 40–50mV hyperpolarized to that of the N-currents (Nowycky et al., 1985). Notably, all three T-type channel subtypes have been shown to have a similar activation $V_{1/2}$ to I_{cat1} (−44mV and −46mV: Monteil et al., 2000a; Monteil et al., 2000b; Klockner et al., 1999).

Activation occurred on the order of 2–8ms, similar to classical whole cell T-type current (Carbone and Lux, 1984; Coulter et al., 1989) and the CaV3.3 T-channel (Klockner et al., 1999). However, R-type currents (Randall and Tsien, 1997; Soong et al., 1993) and N-type currents (Stea et al., 1999) can also activate at these rates. Deactivation occurred very

quickly, in less than 1.5ms. Although this was much faster than typical T-type current (Huguenard and McCormick, 1992; Randall and Tsien, 1997), both CaV3.1 and CaV3.3 currents display such rapid kinetics (Talavera and Nilius, 2006a; Talavera and Nilius 2006b; Chemin et al., 2001). The R-type and N-type currents can also deactivate similarly (Randall and Tsien, 1997; Buraei et al., 2005).

With $\tau_{inactivation}$ of 40–80ms, I_{cat1} decays rate resembles that of classical whole cell LVA current (Fedulova et al., 1985) and CaV3.3, but is slow compared to CaV3.2 and CaV3.1 (Monteil et al., 2000a; Monteil et al., 2000b; Klockner *et al*. 1999). This inactivation rate is faster than R-type (Randall and Tsien, 1997; Soong et al., 1993) and N-type currents (Stea et al., 1999). Interestingly, reticular thalamic neurons fire low threshold bursts of longer duration than thalamic relay neurons, and this difference is attributed to expression of CaV3.3 versus the faster decaying T-type variants (Huguenard and Prince, 1992; Talley et al., 1999). I_{cat1} time constant of recovery from inactivation ranged from 50–80ms, which was lower than that of the classical T-current (Coulter et al., 1989), cloned T-type channel variants (Perez-Reyes, 2003), and R-current (Randall and Tsien, 1997).

I_{cat1} therefore was most likely a T-type current, with a component most likely comprised of CaV3.3. Indeed, immunohistochemical evidence supports presence of CaV3.1 and CaV3.3 in the OB glomeruli (Talley et al., 1999; Klugbauer et al., 1999). Furthermore, these variants of T-current display less sensitivity to nickel block than CaV3.2 (Lee et al., 1999), which may explain the requirement of high concentrations of extracellular nickel to block the plateau potential itself. Such pharamacological differences also occur between reticular thalamic bursts and thalamic relay bursts based on similar calcium channel expression differences (Joksovic et al., 2005).

As mentioned previously, LVA calcium current was identified in rat GABAergic PGCs (Murphy et al., 2005), with a major component identified as L-type based on sustained time course and sensitivity to dihydropyridines and cadmium, but not to nickel (Murphy et al., 2005). In the same cells, some of which could fire bursts, a transient LVA current was identified that also activated above −60mV. Comparing IV curves, it appears that I_{cat1} inactivates with a similar rate, but may activate at slightly more depolarized potentials. It is possible that this T-current from GABAergic PGCs is represented partially in our study, as we recorded a general population of JGCs. The T-current of dopaminergic PGCs (Pignatelli et al., 2005) has slightly hyperpolarized activation compared to I_{cat1}, with peak current at −35mV and $V_{1/2}$ of −45.3mV. We do not think that this current contributed to I_{cat1} because these cells were spike firing only. The LVA current of bursting mouse ETCs has similar features as I_{cat1}, activating with $V_{1/2}$ of −37.1mV and inactivating with τ_{inact} of −62ms (Liu and Shipley, 2008). Certainly I_{cat1} could partially reflect this current, as ETCs are included in these recordings.

I_{cat2} likely reflected a composite of multiple calcium currents. The activation $V_{1/2}$ (−25 mV) is similar to that of P/Q type currents (Llinas et al., 1989; Sather et al., 1993) rather than L-type currents (Fox et al., 1987). All are found in the olfactory bulb glomerular layer (Ludwig et al., 1997).

Though multicompartment models account better for electrotonic effects, single compartment models have been very useful to explore burst and plateau potential mechanisms in other neurons (McCormick and Huguenard, 1992; Genet and Delord, 2002). Our simulation of plateau potential firing demonstrated that I_{cat1} was necesssary but not sufficient for generating the plateau potential, but still more critical than the other two depolarizing currents (I_{cat2}, I_{Na}). The necessity for I_{cat1} was consistent with the finding that the voltage dependence of the current was similar to that of the plateau potential itself, as

measured experimentally in our prior study (Zhou et al., 2006) and simulated in this study. Additionally, inactivation kinetics of I_{cat1} strongly dictated plateau potential duration. This suggests a mechanism in which T-type currents are dominant, as in thalamic relay neurons (Coulter et al., 1989), trigeminal neurons (Hsiao et al., 1998), and the Purkinje cell (Pouille et al., 2000).

We also found that atypical A-current I_{kt1} was more influential on plateau potential shape than the atypical D-current I_{kt2} and delayed rectifier I_{kt3}. Several factors likely contribute to this. First, compared to I_{kt2}, this current activates at more hyperpolarized membrane potentials to interact with I_{Na} and I_{cat1} in the plateau potential voltage range. Also, this current activates much more quickly than I_{kt2} and thus can influence the action potential. Although I_{kt3} shows equivalent activation in the plateau voltage region, it activates at approximately half the rate of I_{kt1} and the overall slope of its activation curve is lower. It is therefore less poised to influence spike and plateau shape. The importance of the A-current to plateau potential firing has also been demonstrated in cerebellar Purkinje cell (Wang et al., 1991b; Serodio and Rudy, 1998; Wang and Schreurs, 2006). However, Purkinje cell plateau potentials are also more reliant on currents similar to I_{kt2} and I_{kt3}, similar to subthalamic nucleus plateau potentials (Midtgaard, 1995; Otsuka et al., 2001; Genet and Delord, 2002; McKay et al., 2005). This may be related to the unique features of potassium currents in JGCs, as well as the unique properties of I_{cat1} with which I_{kt1} interacts.

As discussed in the accompanying paper (Masurkar and Chen, 2011), the limitations to our study stem from the drawbacks of single electrode voltage clamp (space clamp), the possibility of transmitter-mediated modulation of ionic currents, and recordings from a heterogeneous group of neurons (JGCs) that include different neuron types (ETCs and PGCs). We are however encouraged by the consistency of current measurements and ratios across the large number of neurons targeted, and the similarity between the characteritics of currents recorded here and of those expressed in the OB gomerulus. Lastly, we have noticed little variation in plateau potential generation when all ionotropic and metabotropic glutamatergic and GABAergic input is blocked (data not shown).

5. CONCLUSION

In summary, we demonstrate through current clamp recordings, voltage clamp characterization, and computer simulations, that transient calcium current (I_{cat1}) and transient potassium current (I_{kt1}) are the most critical currents for driving and shaping the plateau potentials of olfactory bulb JGCs. Though this was done with calcium-activated potassium currents minimized, we have shown previously that plateau potential shape is minimally influenced by such conductances (Zhou et al., 2006; Masurkar and Chen, 2011). The voltage dependence, kinetics, and pharmacology of I_{cat1} reflect the calcium channels found in the OB glomerulus, CaV3.1 and CaV3.3.

These findings further suggest that T-type and A-type currents are important loci for controlling and modulating JGC function, and in turn odorant processing in the olfactory glomerulus. Lastly, we have developed the first working model of JGC plateau potentials. This, together with prior models of other PGCs (Pignatelli et al., 2005) and mitral cells (Shen et al., 1999; David et al., 2008), could be used to advance existing simulations of small OB networks (Davison et al., 2003; Rubin and Cleland 2006; Karnup et al., 2006; Migliore and Shepherd 2008) to better reflect the complex glomerular layer processing that contributes to odor information processing in the OB.

Acknowledgments

We thank Dr. G. Shepherd for guidance, Dr. S. Nagayama and Dr. M. Fletcher for critically reading the manuscript, and Dr. W. Xiong for technical assistance. This work was supported by National Institute of Deafness and Other Communication Disorders Grants DC-003918 and DC-009666 (W.C.), DC-000086 and DC-004732 (G. M. Shepherd), and a National Institutes of Health Medical Scientist Training Program Grant (A.M.).

Abbreviations

TEA	tetramethylammonium
MES	methanesulfonate
TTX	tetrodotoxin
EGTA	glycol-bis(2-aminoethylether)-N,N,N′,N′-tetraacetic acid
D-APV	D-2-amino-5-phosphonovaleric acid
CNQX	6-cyano-7-nitroquinoxaline-2,3-dione
AMPA	2-amino-3-(5-methyl-3-oxo-1,2-oxazol-4-yl)propanoic acid
NMDA	N-Methyl-D-aspartic acid
HEPES	4-(2-hydroxyethyl)-1-piperazineethanesulfonic acid
ATP	Adenosine-5′-triphosphate
GTP	Guanosine-5′-triphosphate

6. GLOSSARY

Olfactory bulb	The first area of the brain to receive and process primary olfactory sensory information from olfactory sensory neurons
Glomerulus	A spherical 50–100μm of neuropil and the locus of information transfer between olfactory sensory neurons and output neurons of the olfactory bulb, as well as the site of modulation of this transfer by interneurons. Several hundred glomeruli form the first layer of the olfactory bulb
Mitral cell	An excitatory output neuron of the olfactory bulb, whose axons project to olfactory cortex, and whose dendrites are within the glomerulus and cell body is deep to the glomerular layer
Tufted cell	Another excitatory output neuron of the olfactory bulb, whose soma is more superficial than that of a mitral cell
Juxtglomerular cell	A group of neurons whose cell bodies lie around the border of a glomerulus. They include external tufted, periglomerular, and short axons cells
External tufted cell	The most superficially located tufted cell
Periglomerular cell	A chemical heterogeneous group of interneurons within the glomerular layer show dendrites and axons pariticipate in synaptic interactions with other glomerular processes. They can be GABAergic, dopaminergic, or release other neurotransmitters
Short axon cell	An excitatory interneuron thought mediate interglomerular inhibition

References

Antal M, Eyre M, Finklea B, Nusser Z. External tufted cells in the main olfactory bulb form two distinct subpopulations. Eur J Neurosci. 2006; 24:1124–1136. [PubMed: 16930438]

Avery RB, Johnston D. Ca2+ channel antagonist U-92032 inhibits both T-type Ca2+ channels and Na + channels in hippocampal CA1 pyramidal neurons. J Neurophysiol. 1997; 77:1023–1028. [PubMed: 9065866]

Beurrier C, Congar P, Bioulac B, Hammond C. Subthalamic nucleus neurons switch from single-spike activity to burst-firing mode. J Neurosci. 1999; 19:599–609. [PubMed: 9880580]

Buraei Z, Anghelescu M, Elmslie KS. Slowed N-type calcium channel (CaV2.2) deactivation by the cyclin-dependent kinase inhibitor roscovitine. Biophys J. 2005; 89:1681–1691. [PubMed: 15951378]

Cadetti L, Belluzzi O. Hyperpolarisation-activated current in glomerular cells of the rat olfactory bulb. Neuroreport. 2001; 12:3117–3120. [PubMed: 11568648]

Carbone E, Lux HD. A low voltage-activated, fully inactivating Ca channel in vertebrate sensory neurones. Nature. 1984; 310:501–502. [PubMed: 6087159]

Chemin J, Monteil A, Dubel S, Nargeot J, Lory P. The alpha1I T-type calcium channel exhibits faster gating properties when overexpressed in neuroblastoma/glioma NG 108–15 cells. Eur J Neurosci. 2001; 14:1678–1686. [PubMed: 11860462]

Connor JA, Stevens CF. Prediction of repetitive firing behaviour from voltage clamp data on an isolated neurone soma. J Physiol. 1971; 213:31–53. [PubMed: 5575343]

Coulter DA, Huguenard JR, Prince DA. Calcium currents in rat thalamocortical relay neurones: kinetic properties of the transient, low-threshold current. J Physiol. 1989; 414:587–604. [PubMed: 2607443]

David F, Linster C, Cleland TA. Lateral dendritic shunt inhibition can regularize mitral cell spike patterning. J Comput Neurosci. 2008; 25:25–38. [PubMed: 18060489]

Davison AP, Feng J, Brown D. Dendrodendritic inhibition and simulated odor responses in a detailed olfactory bulb network model. J Neurophysiol. 2003; 90:1921–1935. [PubMed: 12736241]

De Saint Jan D, Hirnet D, Westbrook GL, Charpak S. External tufted cells drive the output of olfactory bulb glomeruli. J Neurosci. 2009; 29:2043–2052. [PubMed: 19228958]

De Schutter E, Bower JM. An active membrane model of the cerebellar Purkinje cell. I. Simulation of current clamps in slice. J Neurophysiol. 1994; 71:375–400. [PubMed: 7512629]

Fedulova SA, Kostyuk PG, Veselovsky NS. Two types of calcium channels in the somatic membrane of new-born rat dorsal root ganglion neurones. J Physiol. 1985; 359:431–446. [PubMed: 2582115]

Fox AP, Nowycky MC, Tsien RW. Kinetic and pharmacological properties distinguishing three types of calcium currents in chick sensory neurones. J Physiol. 1987; 394:149–172. [PubMed: 2451016]

Fraser DD, MacVicar BA. Cholinergic-dependent plateau potential in hippocampal CA1 pyramidal neurons. J Neurosci. 1996; 16:4113–4128. [PubMed: 8753873]

Genet S, Delord B. A biophysical model of nonlinear dynamics underlying plateau potentials and calcium spikes in purkinje cell dendrites. J Neurophysiol. 2002; 88:2430–2444. [PubMed: 12424284]

Gire DH, Schoppa NE. Control of on/off glomerular signaling by a local GABAergic microcircuit in the olfactory bulb. J Neurosci. 2009; 29:13454–13464. [PubMed: 19864558]

Goldman DE. Potential, impedance, and rectification in membranes. J Gen Physiol. 1943; 27:37–60. [PubMed: 19873371]

Hagiwara S, Ozawa S, Sand O. Voltage clamp analysis of two inward current mechanisms in the egg cell membrane of a starfish. J Gen Physiol. 1975; 65:617–644. [PubMed: 240906]

Hayar A, Karnup S, Ennis M, Shipley MT. External tufted cells: a major excitatory element that coordinates glomerular activity. J Neurosci. 2004; 24:6676–6685. [PubMed: 15282270]

Hayar A, Karnup S, Shipley MT, Ennis M. Olfactory bulb glomeruli: external tufted cells intrinsically burst at theta frequency and are entrained by patterned olfactory input. J Neurosci. 2004; 24:1190–1199. [PubMed: 14762137]

Hayar A, Shipley MT, Ennis M. Olfactory bulb external tufted cells are synchronized by multiple intraglomerular mechanisms. J Neurosci. 2005; 25:8197–8208. [PubMed: 16148227]

Hines ML, Carnevale NT. The NEURON simulation environment. Neural Comput. 1997; 9:1179–1209. [PubMed: 9248061]

Hodgkin AL, Huxley AF. A quantitative description of membrane current and its application to conduction and excitation in nerve. J Physiol. 1952; 117:500–544. [PubMed: 12991237]

Hodgkin AL, Katz B. The effect of sodium ions on the electrical activity of the giant axon of the squid. J Physiol. 1949; 108:37–77. [PubMed: 18128147]

Hounsgaard J, Mintz I. Calcium conductance and firing properties of spinal motoneurones in the turtle. J Physiol. 1988; 398:591–603. [PubMed: 2455804]

Hsiao CF, Del Negro CA, Trueblood PR, Chandler SH. Ionic basis for serotonin-induced bistable membrane properties in guinea pig trigeminal motoneurons. J Neurophysiol. 1998; 79:2847–2856. [PubMed: 9636091]

Huguenard JR, McCormick DA. Simulation of the currents involved in rhythmic oscillations in thalamic relay neurons. J Neurophysiol. 1992; 68:1373–1383. [PubMed: 1279135]

Huguenard JR, Prince DA. A novel T-type current underlies prolonged Ca(2+)-dependent burst firing in GABAergic neurons of rat thalamic reticular nucleus. J Neurosci. 1992; 12:3804–3817. [PubMed: 1403085]

Jaffe DB, Ross WN, Lisman JE, Lasser-Ross N, Miyakawa H, Johnston D. A model for dendritic Ca2+ accumulation in hippocampal pyramidal neurons based on fluorescence imaging measurements. J Neurophysiol. 1994; 71:1065–1077. [PubMed: 8201402]

Jahnsen H, Llinas R. Electrophysiological properties of guinea-pig thalamic neurones: an in vitro study. J Physiol. 1984; 349:205–226. [PubMed: 6737292]

Jahnsen H, Llinas R. Ionic basis for the electro-responsiveness and oscillatory properties of guinea-pig thalamic neurones in vitro. J Physiol. 1984; 349:227–247. [PubMed: 6737293]

Johnson BA, Leon M. Modular representations of odorants in the glomerular layer of the rat olfactory bulb and the effects of stimulus concentration. J Comp Neurol. 2000; 422:496–509. [PubMed: 10861522]

Joksovic PM, Bayliss DA, Todorovic SM. Different kinetic properties of two T-type Ca2+ currents of rat reticular thalamic neurones and their modulation by enflurane. J Physiol. 2005; 566:125–142. [PubMed: 15845580]

Karnup SV, Hayar A, Shipley MT, Kurnikova MG. Spontaneous field potentials in the glomeruli of the olfactory bulb: the leading role of juxtaglomerular cells. Neuroscience. 2006; 142:203–221. [PubMed: 16876327]

Kay AR, Sugimori M, Llinas R. Kinetic and stochastic properties of a persistent sodium current in mature guinea pig cerebellar Purkinje cells. J Neurophysiol. 1998; 80:1167–1179. [PubMed: 9744930]

Klockner U, Lee JH, Cribbs LL, Daud A, Hescheler J, Pereverzev A, Perez-Reyes E, Schneider T. Comparison of the Ca2 + currents induced by expression of three cloned alpha1 subunits, alpha1G, alpha1H and alpha1I, of low-voltage-activated T-type Ca2 + channels. Eur J Neurosci. 1999; 11:4171–4178. [PubMed: 10594642]

Klugbauer N, Marais E, Lacinova L, Hofmann F. A T-type calcium channel from mouse brain. Pflugers Arch. 1999; 437:710–715. [PubMed: 10087148]

Kosaka K, Kosaka T. synaptic organization of the glomerulus in the main olfactory bulb: compartments of the glomerulus and heterogeneity of the periglomerular cells. Anat Sci Int. 2005; 80:80–90. [PubMed: 15960313]

Kuzmiski JB, Barr W, Zamponi GW, MacVicar BA. Topiramate inhibits the initiation of plateau potentials in CA1 neurons by depressing R-type calcium channels. Epilepsia. 2005; 46:481–489. [PubMed: 15816941]

Lee JH, Gomora JC, Cribbs LL, Perez-Reyes E. Nickel block of three cloned T-type calcium channels: low concentrations selectively block alpha1H. Biophys J. 1999; 77:3034–3042. [PubMed: 10585925]

Lee SC, Hayashida Y, Ishida AT. Availability of low-threshold Ca2+ current in retinal ganglion cells. J Neurophysiol. 2003; 90:3888–3901. [PubMed: 14665686]

Li Y, Bennett DJ. Persistent sodium and calcium currents cause plateau potentials in motoneurons of chronic spinal rats. J Neurophysiol. 2003; 90:857–869. [PubMed: 12724367]

Liu S, Shipley MT. Multiple conductances cooperatively regulate spontaneous bursting in mouse olfactory bulb external tufted cells. J Neurosci. 2008; 28:1625–1639. [PubMed: 18272683]

Llinas R, Sugimori M, Lin JW, Cherksey B. Blocking and isolation of a calcium channel from neurons in mammals and cephalopods utilizing a toxin fraction (FTX) from funnel-web spider poison. Proc Natl Acad Sci U S A. 1989; 86:1689–1693. [PubMed: 2537980]

Ludwig A, Flockerzi V, Hofmann F. Regional expression and cellular localization of the alpha1 and beta subunit of high voltage-activated calcium channels in rat brain. J Neurosci. 1997; 17:1339–1349. [PubMed: 9006977]

Mainen ZF, Joerges J, Huguenard JR, Sejnowski TJ. A model of spike initiation in neocortical pyramidal neurons. Neuron. 1995; 15:1427–1439. [PubMed: 8845165]

McCormick DA, Huguenard JR. A model of the electrophysiological properties of thalamocortical relay neurons. J Neurophysiol. 1992; 68:1384–1400. [PubMed: 1331356]

McKay BE, Molineux ML, Mehaffey WH, Turner RW. Kv1 K+ channels control Purkinje cell output to facilitate postsynaptic rebound discharge in deep cerebellar neurons. J Neurosci. 2005; 25:1481–1492. [PubMed: 15703402]

McQuiston AR, Katz LC. Electrophysiology of interneurons in the glomerular layer of the rat olfactory bulb. J Neurophysiol. 2001; 86:1899–1907. [PubMed: 11600649]

Midtgaard J. Spatial synaptic integration in Purkinje cell dendrites. J Physiol Paris. 1995; 89:23–32. [PubMed: 7581295]

Migliore M, Shepherd GM. Dendritic action potentials connect distributed dendrodendritic microcircuits. J Comput Neurosci. 2008; 24:207–221. [PubMed: 17674173]

Mombaerts P, Wang F, Dulac C, Chao SK, Nemes A, Mendelsohn M, Edmondson J, Axel R. Visualizing an olfactory sensory map. Cell. 1996; 87:675–686. [PubMed: 8929536]

Monteil A, Chemin J, Bourinet E, Mennessier G, Lory P, Nargeot J. Molecular and functional properties of the human alpha(1G) subunit that forms T-type calcium channels. J Biol Chem. 2000; 275:6090–6100. [PubMed: 10692398]

Monteil A, Chemin J, Leuranguer V, Altier C, Mennessier G, Bourinet E, Lory P, Nargeot J. Specific properties of T-type calcium channels generated by the human alpha 1I subunit. J Biol Chem. 2000; 275:16530–16535. [PubMed: 10749850]

Mori K, Nagao H, Yoshihara Y. The olfactory bulb: coding and processing of odor molecule information. Science. 1999; 286:711–715. [PubMed: 10531048]

Murphy GJ, Darcy DP, Isaacson JS. Intraglomerular inhibition: signaling mechanisms of an olfactory microcircuit. Nat Neurosci. 2005; 8:354–364. [PubMed: 15696160]

Neher E. Correction for liquid junction potentials in patch clamp experiments. Methods Enzymol. 1992; 207:123–131. [PubMed: 1528115]

Nowycky MC, Fox AP, Tsien RW. Three types of neuronal calcium channel with different calcium agonist sensitivity. Nature. 1985; 316:440–443. [PubMed: 2410796]

Otsuka T, Murakami F, Song WJ. Excitatory postsynaptic potentials trigger a plateau potential in rat subthalamic neurons at hyperpolarized states. J Neurophysiol. 2001; 86:1816–1825. [PubMed: 11600642]

Partridge LD, Muller TH, Swandulla D. Calcium-activated non-selective channels in the nervous system. Brain Res Brain Res Rev. 1994; 19:319–325. [PubMed: 7820135]

Perez-Reyes E. Molecular physiology of low-voltage-activated t-type calcium channels. Physiol Rev. 2003; 83:117–161. [PubMed: 12506128]

Pignatelli A, Kobayashi K, Okano H, Belluzzi O. Functional properties of dopaminergic neurones in the mouse olfactory bulb. J Physiol. 2005; 564:501–514. [PubMed: 15731185]

Pinching AJ, Powell TP. The neuron types of the glomerular layer of the olfactory bulb. J Cell Sci. 1971; 9:305–345. [PubMed: 4108056]

Pinching AJ, Powell TP. The neuropil of the glomeruli of the olfactory bulb. J Cell Sci. 1971; 9:347–377. [PubMed: 4108057]

Pinching AJ, Powell TP. The neuropil of the periglomerular region of the olfactory bulb. J Cell Sci. 1971; 9:379–409. [PubMed: 5124504]

Plummer MR, Hess P. Reversible uncoupling of inactivation in N-type calcium channels. Nature. 1991; 351:657–659. [PubMed: 1646965]

Pouille F, Cavelier P, Desplantez T, Beekenkamp H, Craig PJ, Beattie RE, Volsen SG, Bossu JL. Dendro-somatic distribution of calcium-mediated electrogenesis in purkinje cells from rat cerebellar slice cultures. J Physiol. 2000; 527(Pt 2):265–282. [PubMed: 10970428]

Randall AD, Tsien RW. Contrasting biophysical and pharmacological properties of T-type and R-type calcium channels. Neuropharmacology. 1997; 36:879–893. [PubMed: 9257934]

Ressler KJ, Sullivan SL, Buck LB. Information coding in the olfactory system: evidence for a stereotyped and highly organized epitope map in the olfactory bulb. Cell. 1994; 79:1245–1255. [PubMed: 7528109]

Rubin BD, Katz LC. Optical imaging of odorant representations in the mammalian olfactory bulb. Neuron. 1999; 23:499–511. [PubMed: 10433262]

Rubin DB, Cleland TA. Dynamical mechanisms of odor processing in olfactory bulb mitral cells. J Neurophysiol. 2006; 96:555–568. [PubMed: 16707721]

Sather WA, Tanabe T, Zhang JF, Mori Y, Adams ME, Tsien RW. Distinctive biophysical and pharmacological properties of class A (BI) calcium channel alpha 1 subunits. Neuron. 1993; 11:291–303. [PubMed: 8394721]

Serodio P, Rudy B. Differential expression of Kv4 K+ channel subunits mediating subthreshold transient K+ (A-type) currents in rat brain. J Neurophysiol. 1998; 79:1081–1091. [PubMed: 9463463]

Shen GY, Chen WR, Midtgaard J, Shepherd GM, Hines ML. Computational analysis of action potential initiation in mitral cell soma and dendrites based on dual patch recordings. J Neurophysiol. 1999; 82:3006–3020. [PubMed: 10601436]

Shepherd, GM., et al. Olfactory Bulb. In: Shepherd, GM., editor. Synaptic Organization of the Brain. New York: Oxford; 2004. p. 165-216.

Shipley MT, Ennis M. Functional organization of olfactory system. J Neurobiol. 1996; 30:123–176. [PubMed: 8727988]

Soong TW, Stea A, Hodson CD, Dubel SJ, Vincent SR, Snutch TP. Structure and functional expression of a member of the low voltage-activated calcium channel family. Science. 1993; 260:1133–1136. [PubMed: 8388125]

Stea A, Dubel SJ, Snutch TP. alpha 1B N-type calcium channel isoforms with distinct biophysical properties. Ann N Y Acad Sci. 1999; 868:118–130. [PubMed: 10414290]

Stewart WB, Kauer JS, Shepherd GM. Functional organization of rat olfactory bulb analysed by the 2-deoxyglucose method. J Comp Neurol. 1979; 185:715–734. [PubMed: 447878]

Talavera K, Nilius B. Biophysics and structure-function relationship of T-type Ca2+ channels. Cell Calcium. 2006; 40:97–114. [PubMed: 16777221]

Talavera K, Nilius B. Evidence for common structural determinants of activation and inactivation in T-type Ca2+ channels. Pflugers Arch. 2006; 453:189–201. [PubMed: 16955311]

Talbot MJ, Sayer RJ. Intracellular QX-314 inhibits calcium currents in hippocampal CA1 pyramidal neurons. J Neurophysiol. 1996; 76:2120–2124. [PubMed: 8890325]

Talley EM, Cribbs LL, Lee JH, Daud A, Perez-Reyes E, Bayliss DA. Differential distribution of three members of a gene family encoding low voltage-activated (T-type) calcium channels. J Neurosci. 1999; 19:1895–1911. [PubMed: 10066243]

Traub RD, Buhl EH, Gloveli T, Whittington MA. Fast rhythmic bursting can be induced in layer 2/3 cortical neurons by enhancing persistent Na+ conductance or by blocking BK channels. J Neurophysiol. 2003; 89:909–921. [PubMed: 12574468]

Vassar R, Chao SK, Sitcheran R, Nunez JM, Vosshall LB, Axel R. Topographic organization of sensory projections to the olfactory bulb. Cell. 1994; 79:981–991. [PubMed: 8001145]

Wang D, Schreurs BG. Characteristics of IA currents in adult rabbit cerebellar Purkinje cells. Brain Res. 2006; 1096:85–96. [PubMed: 16716270]

Wang XJ, Rinzel J, Rogawski MA. A model of the T-type calcium current and the low-threshold spike in thalamic neurons. J Neurophysiol. 1991; 66:839–850. [PubMed: 1661326]

Wang Y, Strahlendorf JC, Strahlendorf HK. A transient voltage-dependent outward potassium current in mammalian cerebellar Purkinje cells. Brain Res. 1991; 567:153–158. [PubMed: 1815823]

Wellis DP, Scott JW. Intracellular responses of identified rat olfactory bulb interneurons to electrical and odor stimulation. J Neurophysiol. 1990; 64:932–947. [PubMed: 2230935]

Xu F, Liu N, Kida I, Rothman DL, Hyder F, Shepherd GM. Odor maps of aldehydes and esters revealed by functional MRI in the glomerular layer of the mouse olfactory bulb. Proc Natl Acad Sci U S A. 2003; 100:11029–11034. [PubMed: 12963819]

Yoshida S, Matsuda Y. Studies on sensory neurons of the mouse with intracellular-recording and horseradish peroxidase-injection techniques. J Neurophysiol. 1979; 42:1134–1145. [PubMed: 479922]

Zamponi GW, Bourinet E, Snutch TP. Nickel block of a family of neuronal calcium channels: subtype- and subunit-dependent action at multiple sites. J Membr Biol. 1996; 151:77–90. [PubMed: 8661496]

Zhou Z, Xiong W, Masurkar AV, Chen WR, Shepherd GM. Dendritic calcium plateau potentials modulate input-output properties of juxtaglomerular cells in the rat olfactory bulb. J Neurophysiol. 2006; 96:2354–2363. [PubMed: 16855116]

RESEARCH HIGHLIGHTS

- Olfactory juxtaglomerular cells fire plateau potentials of unclear mechanism.
- We recorded their calcium current, showing a transient and sustained component.
- We created a model of plateau potential firing based on these recordings.
- The model showed that transient calcium current generates the plateau potential.
- The model also showed that transient potassium current is also critical.

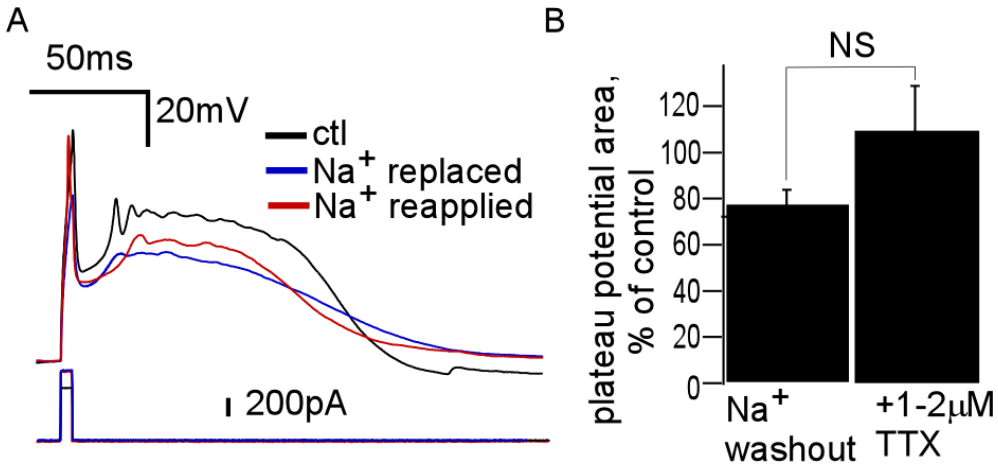

Figure 1. Role of Na^+ ions in JGC plateau potential firing

(A) JGC plateau potential before (black) and after replacement (blue) of extracellular Na^+ with $Tris^+$, with return of action potential after extracellular sodium reapplication (red) (n = 8). (**B)** Average remaining plateau potential area, as percent of control, after reduction of Na^+ by Na^+ replacement (left) and pharmacological blockade of Na^+ channels (right) with extracellular TTX (n = 10, p = 0.15).

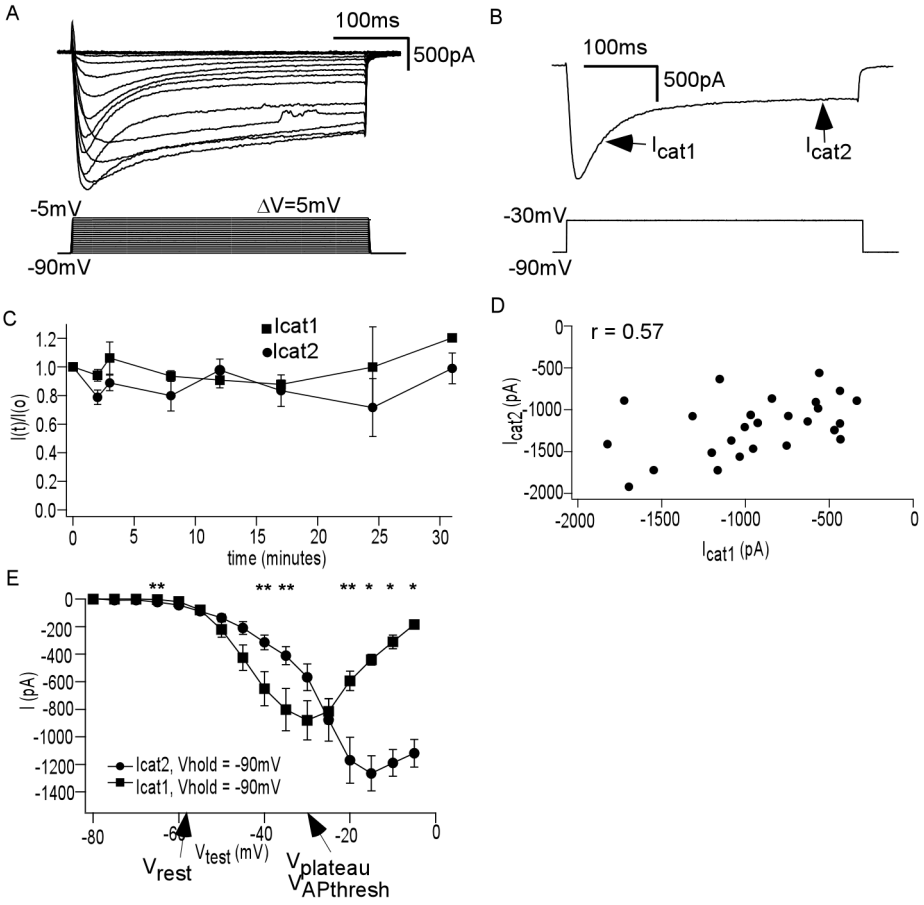

Figure 2. Ca^{2+} current (I_{Ca}) of JGCs: rapidly inactivating I_{cat1} and very slowly inactivating I_{cat2}

(A) I_{Ca} (above) elicited by step depolarizations of 5mV from −90mV (below) (n = 14) (**B)** At test potential of −30mV, I_{Ca} clearly had a rapidly inactivating (I_{cat1}) and a more sustained (I_{cat2}) component. (**C)** Ratios of each current's amplitude in time to its amplitude at the beginning of recording indicate stability of recording to 31 minutes (n = 12) (**D)** Plot of maximum I_{cat1} and I_{cat2} in each cell recorded indicate no consistent ratio (n = 27, Pearson r = 0.57). (**E)** Average current-voltage curves, from protocol as in Figure 2A, for I_{cat1} (square) and I_{cat2} (circle), show distinct relationships. Key plateau potential shape parameters are noted (n = 8, * $p<0.0005$, ** $p<0.05$)

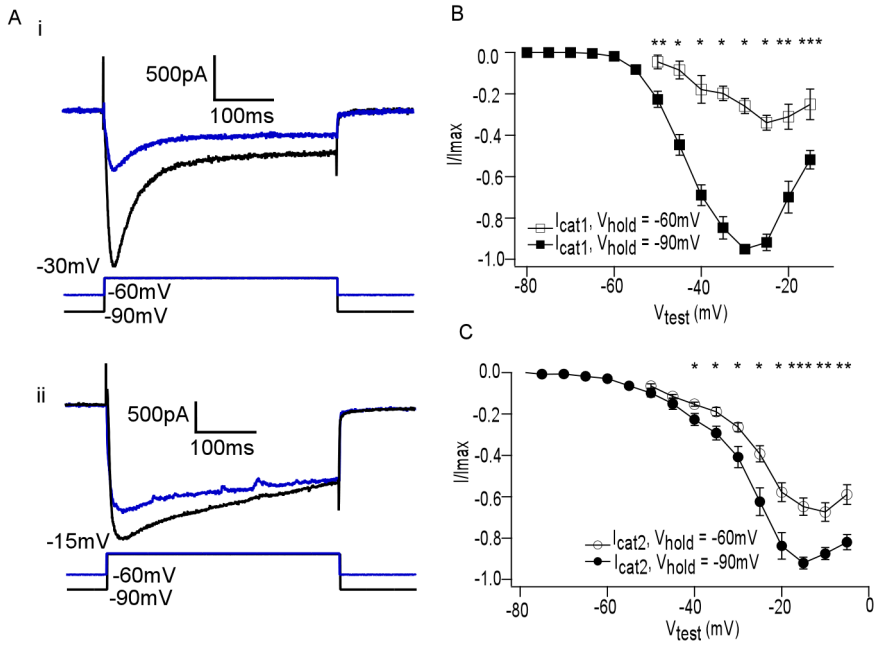

Figure 3. I_{cat1} is more sensitive than I_{cat2} to steady state voltage changes

(A) (i) I_{ca} elicited by a −30mV test potential, at which I_{cat1} had peak activation, from two different holding potentials V_{hold}: −90mV (black) and −60mV (blue). **(ii)** I_{ca} elicited by a −30mV test potential, at which I_{cat2} had peak activation, from two different holding potentials V_{hold}: −90mV (black) and −60mV (blue) (n = 8; *p<0.002, **p<0.005, ***p<0.02). (**B)** Plot of average normalized I_{cat1} versus test potential (V_{test}), repeated at two values of V_{hold}, shows dependence on steady state holding potential **(C)** Plot of average normalized I_{cat2} versus test potential (V_{test}), repeated at two values of V_{hold}, shows less dependence on steady state holding potential (n = 8, *p<0.05, **p<0.005, ***p<0.0005)

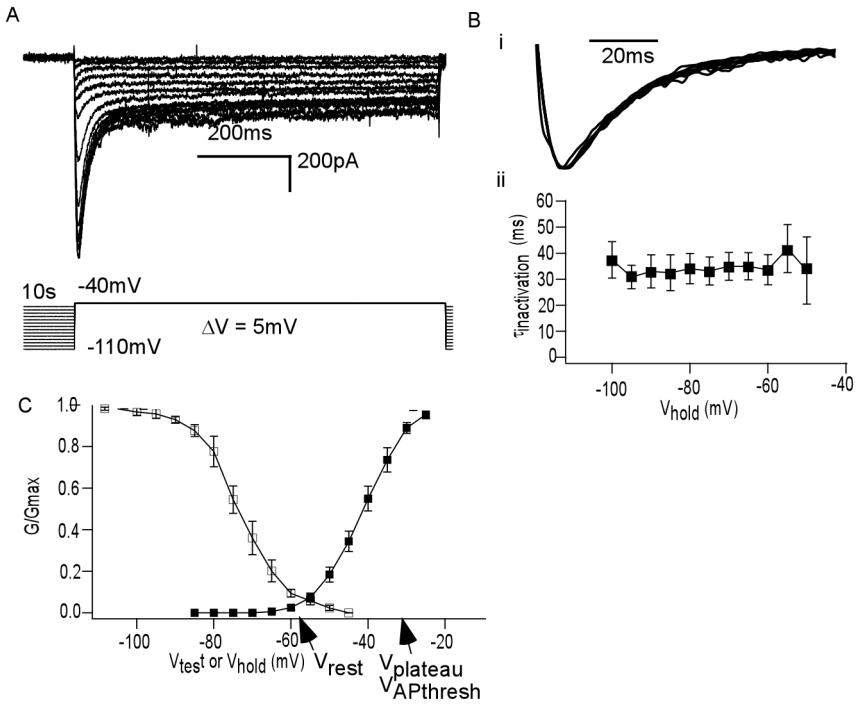

Figure 4. I_{cat1} displays smooth steady state inactivation and activation

(A) I_{Ca} (above) elicited by inactivation protocol (below) in which V_{hold} was varied for a given V_{test} (**B) (i)** Superimposed normalized I_{cat1} traces from a single inactivation protocol shows overlap (**ii)** Plot of time constant of inactivation ($\tau_{inactivation}$) of I_{cat1} elicited at each V_{hold}, averaged over many cells, shows consistency over holding potentials (**C)** Plot of steady state inactivation versus V_{hold}, derived from data in Figure 4A. Superimposed is steady state activation versus V_{test}, derived from IV curve of Figure 2E. Key plateau potential shape parameters are noted.

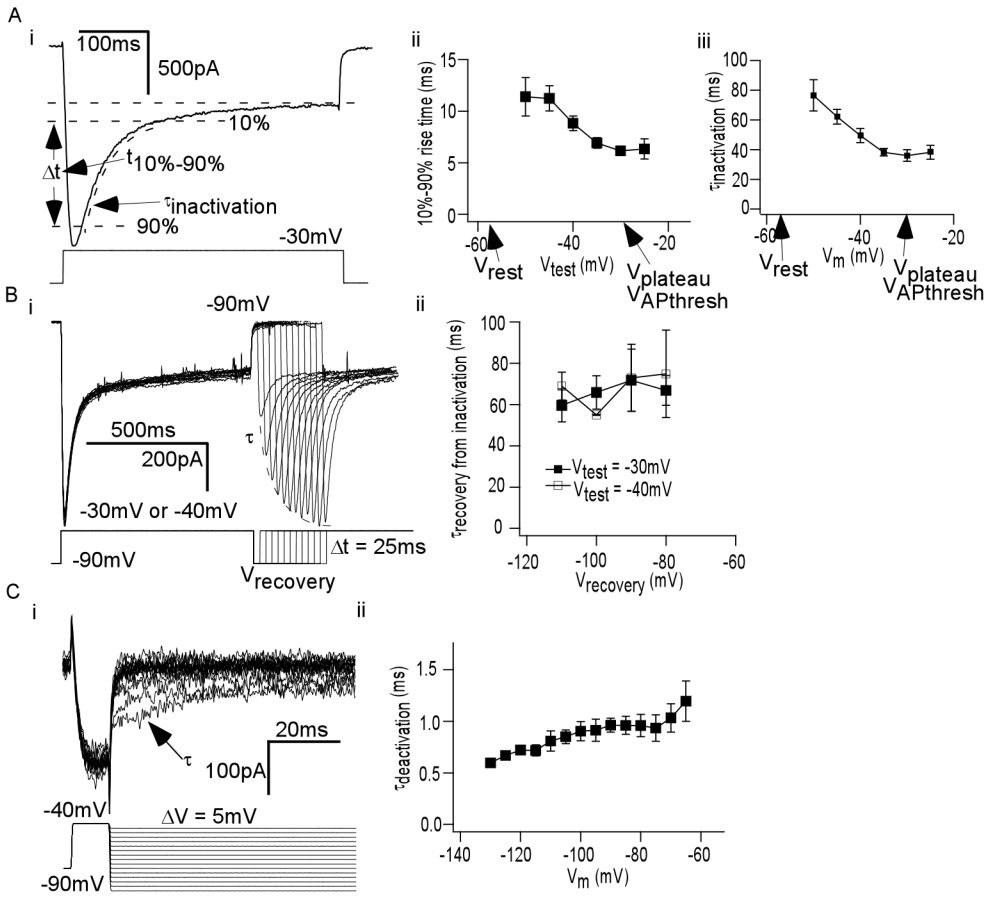

Figure 5. Kinetics of I_{cat1}

(A) (i) 10%–90% rise time and $\tau_{inactivation}$ were extrapolated as shown from currents elicited as in Figure 2A **(ii)** Plot of 10%–90% rise time versus V_{test}. **(iii)** Plot of $\tau_{inactivation}$ versus V_{test}. Key plateau potential shape parameters are noted. (**B) (i)** I_{Ca} (above) elicited from voltage protocol (below) to study I_{cat1} recovery from inactivation **(ii)** Plot of $\tau_{recovery\ from\ nactivation}$ of I_{cat1} versus recovery potential ($V_{recovery}$), at two values of V_{test}: −30mV (filled square) and −40mV (open square) (**C) (i)** I_{Ca} (above) elicited from voltage protocol (below) to study time constant of deactivation ($\tau_{deactivation}$) for I_{cat1} **(ii)** Plot of $\tau_{deactivation}$ versus $V_{repolarization}$.

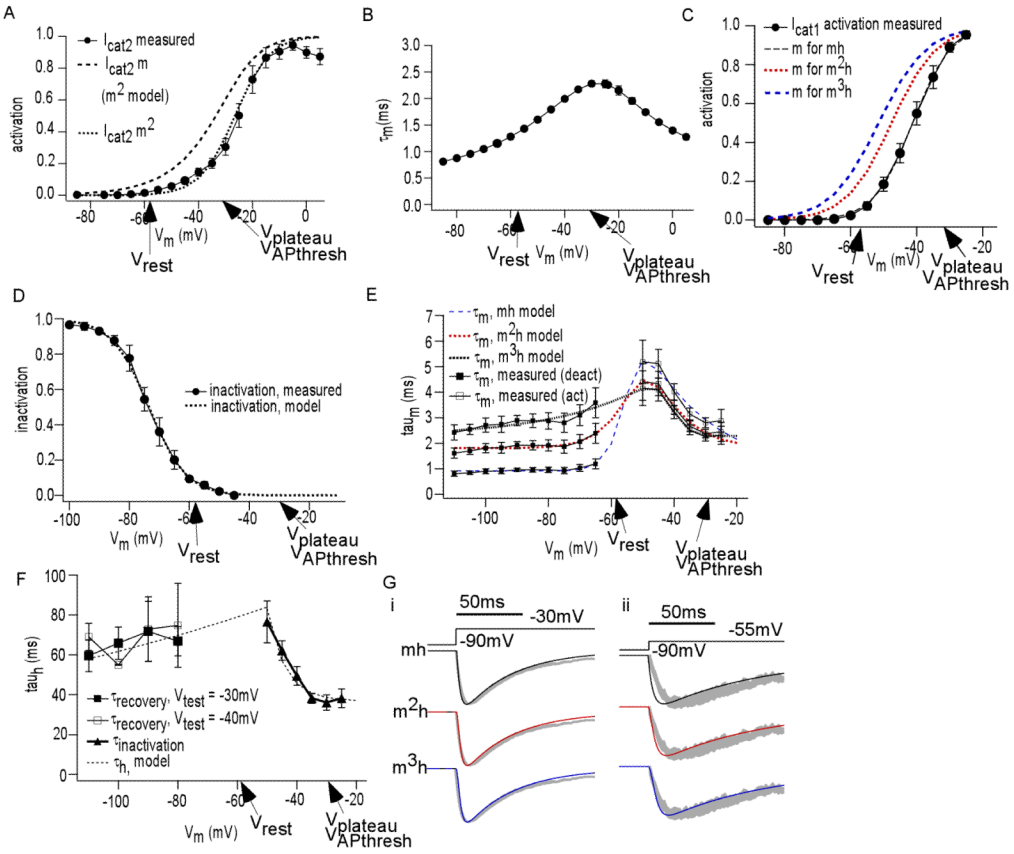

Figure 6. Simulation of I_{cat2} and I_{cat1}

(A) (i) Steady state activation of I_{cat2} versus V_{test}, derived from Figure 2E. Superimposed is I_{cat2} $m_\infty(V_m)$ (broad dash). Its square, I_{cat2} $m_\infty^2(V_m)$ (fine dash), overlaps the experimental activation curve (solid line). Function modified from Traub et al., 2003. (**B**) Time constant of activation (τ_m) as function of V_m for I_{cat2} (Traub et al., 2003) (**C**) Three Boltzmann functions $m_\infty(V_m)$ (m – black dash, m^2 – red dash, m^3 – blue dash) that, when raised to the appropriate power (1,2,3), all closely fit the measured activation curve of I_{cat1} (solid line). For clarity, each is shown prior to this exponentiation. (**D**) Boltzmann function $h_\infty(V_m)$ and measured steady state inactivation of I_{cat1}. This was used for all three I_{cat1} models (mh, m^2h, m^3h). (**E**) Experimental $\tau_{activation}$ (open square) and $\tau_{deactivation}$ (filled square), as functions of V_m, were both scaled appropriately for each of the three schemes (see Methods and Figures 5A, 5C). Superimposed are three $\tau_m(Vm)$ curves, fit to these scaled experimental data (m – black, m^2 – red, m^3 – blue). These were used for each I_{cat1} model (mh, m^2h, m^3h). (**F**) Experimental $\tau_{inactivation}$ and $\tau_{recovery\ from\ inactivation}$, as functions of V_m (see Figures 5A, 5B). Superimposed is $\tau_h(Vm)$ fit, used in all I_{cat1} models (mh, m^2h, m^3h) (**G**) Three models were generated from descriptions in 6A–F. **(i)** Simulated I_{cat1} evoked by V_{test} of −30mV, using each scheme (mh - black, m^2h - red, m^3h - blue). Superimposed (gray) is average experimentally recorded I_{cat1} at this V_{test}. The m^3h scheme shows the best fit. (**ii)** Simulated I_{cat1} evoked by Vtest of −55mV, using each scheme (mh - black, m^2h - red, m^3h - blue). Superimposed (gray) is experimentally recorded I_{cat1} at this V_{test}. The m^3h scheme shows the best fit. Key plateau potential shape parameters are noted throughout.

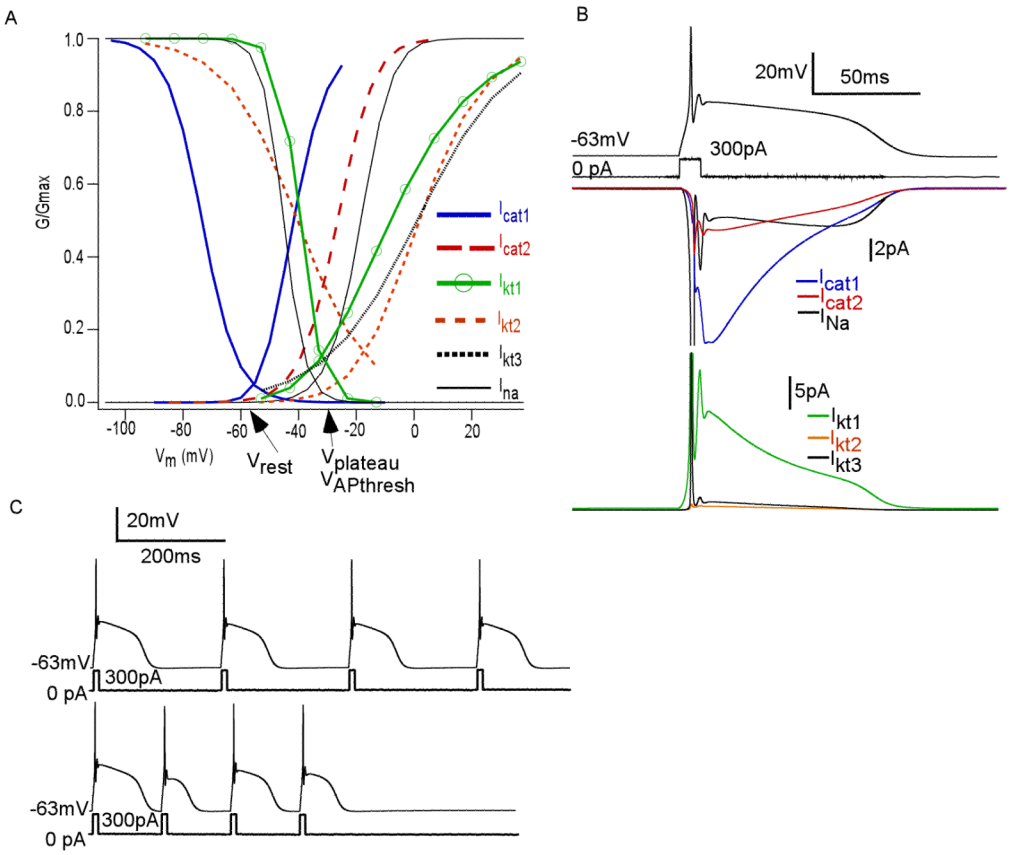

Figure 7. Simulation of JGC plateau potentials

(A) Summary of all $m_{\infty}(V_m)$ and $h_{\infty}(V_m)$ curves for the 6 currents used for the simulation (**B)** The multiconductance model well simulates a plateau potential in response to current input (top). Time courses of inward currents (middle) and outward currents (bottom) are shown. Note prominance of I_{cat1} (blue - middle) and I_{kt1} (green - bottom) during the plateau (**C)** The model preserves intrinsic frequency preference of recurrent plateau potentials, as evidenced by consistently shaped plateau potentials with current injection every 240ms (above) but not when every 130ms (below).

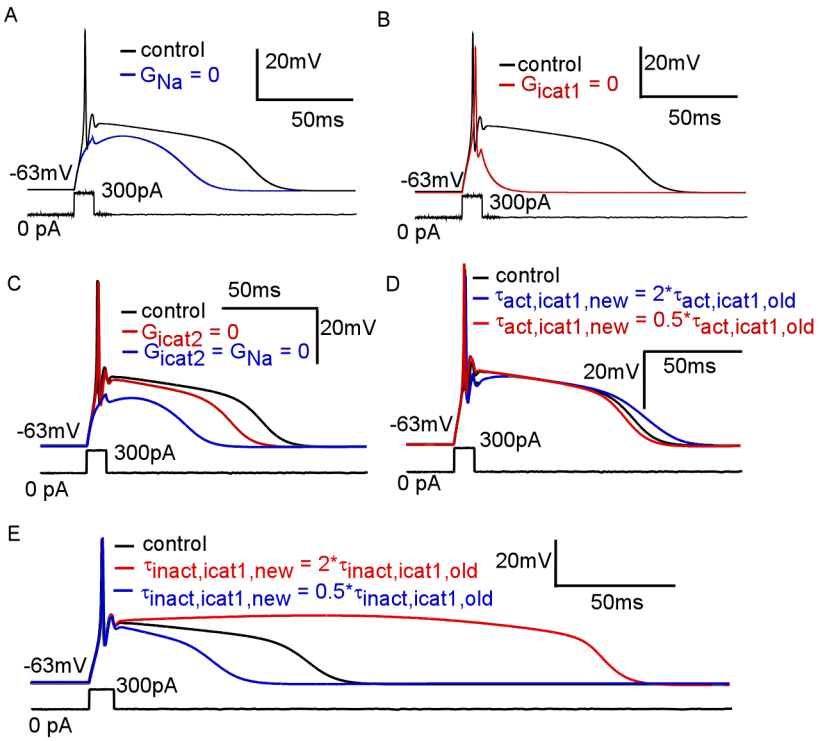

Figure 8. Role of inward currents in JGC plateau potentials

(A) Response of simulated JGC to current injection before (black) and after (blue) removal of sodium conductance shows persistence of a depolarizing potential (**B)** Model response to current injection before (black) and after (red) removal of I_{cat1} conductance shows critical dependence on I_{cat1} (**C)** Simulated JGC plateau potential (black), after removal of I_{cat2} conductance (red), and after removal of both I_{cat2} and I_{Na} conductances (blue) shows persistence of a small depolarizing potential (**D)** JGC plateau potential simulation with I_{cat1} $\tau_{activation}$ at control values (black), increased by factor of 2 (blue), and decreased by factor of 2 (red) shows some dependence of plateau duration on I_{cat1} activation kinetics (**E**) JGC plateau potential simulation with $\tau_{inactivation}$ at control values (black), increased by factor of 2 (red), and decreased by factor of 2 (blue), demonstrates significant dependence of plaeau duration on I_{kt1} inactivation kinetics

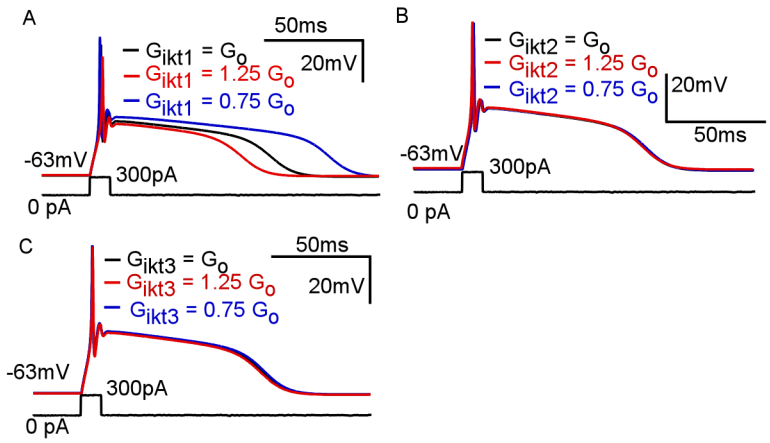

Figure 9. Role of potassium currents in plateau potential generation

(A) Simulated JGC plateau potential (black), after increasing I_{kt1} conductance by 25% (red), and after decreasing I_{kt1} conductance by 25% (blue) demonstrates dependence of plateau duration on this conductance magnitude (**B)** Simulated JGC plateau potential (black), after increasing I_{kt2} conductance by 25% (red), and after decreasing I_{kt2} conductance by 25% (blue) shows almost no variation (**C)** Simulated JGC plateau potential (black), after increasing I_{kt3} conductance by 25% (red), and after decreasing I_{kt3} conductance by 25% (blue), also shows almost no variation.

Table 1

Activation equations for models of JGC calcium, sodium, and potassium currents

	scheme	$m_{inf}(V_m)$	$t_m(V_m)$
I_{cat1}	m^3h	$\frac{1}{1+e^{\frac{-(Vm+51.44)}{7.23}}}$	$\frac{1}{(e^{(\frac{V_m+68.03}{-27.68})}+e^{(\frac{V_m+39.08}{2.74})})}+2.29$
I_{cat2}	m^2	$\frac{\alpha(V_m)}{\alpha(V_m)+\beta(V_m)}$	$\frac{1}{\alpha(V_m)+\beta(V_m)}$
		$\alpha(V_m)=\frac{1.11}{1+e^{(-0.058(V_m+10))}}$	
		$\beta(V_m)=\frac{0.02(V_m+23.9)}{e^{\frac{(Vm+23.9)}{5}}-1}$	
I_{Na}	m^3h	$\frac{\alpha(V_m)}{\alpha(V_m)+\beta(V_m)}$	$\frac{1}{\alpha(V_m)+\beta(V_m)}$
		$\alpha(V_m)=\frac{0.242621(V_m+67.3833)}{1-e^{\frac{-(V_m+67.3833)}{3.51809}}}$	
		$\beta(V_m)=\frac{0.819229(-V_m-18.8432)}{1-e^{\frac{(V_m+18.8432)}{3.9834}}}$	
I_{kt1}	m^4h	$\frac{1}{1+e^{\frac{-(Vm+39.1)}{18.56}}}$	$\frac{e^{(0.17*0.35*(V_m+31.5))}}{0.54(3+e^{(0.17(V_m+31.5))})}+0.23$

scheme	$m_{inf}(V_m)$	$t_m(V_m)$
I_{kt2} m^2h	$\frac{1}{1+e^{\frac{-(Vm+9.83)}{13.18}}}$	$\frac{e^{\frac{(0.562*0.978*(V_m+17.91))}{(0.562(V_m+17.91))}}}{0.2(23+e^{\frac{(0.562(V_m+17.91))}{}})} + 2.45$
I_{kt3} m	$\frac{\alpha(V_m)}{\alpha(V_m)+\beta(V_m)}$	$\frac{1}{\alpha(V_m)+\beta(V_m)}$
	$\alpha(V_m) = \frac{0.6(V_m - 40)}{1 - e^{\frac{-(Vm-40)}{16.7}}}$	
	$\beta(V_m) = \frac{-0.012(V_m - 40)}{1 - e^{\frac{(Vm-40)}{16.7}}}$	

Table 2

Inactivation equations for models of JGC calcium, sodium, and potassium currents

	scheme	$h_{inf}(V_m)$	$\tau_h(V_m)$
I_{cat1}	m^3h	$\frac{1}{1+e^{\frac{(V_m+73.43)}{6.04}}}$	If $V_m < -50mv$: $e^{\frac{(V_m+770)}{162.5}}$ Else : $37+e^{\frac{(V_m+27)}{-6}}$
I_{Na}	m^3h	$\frac{1}{1+e^{\frac{(V_m+45.1801)}{3.73406}}}$	$\frac{1}{\alpha(V_m)+\beta(V_m)}$ $\alpha(V_m)=\frac{0.0802232(V_m+36.1689)}{1-e^{\frac{-(V_m+36.1689)}{5.63879}}}$ $\beta(V_m)=\frac{0.00422366(-V_m-35.4483)}{1-e^{\frac{(V_m+35.4483)}{5.63879}}}$
I_{kt1}	m^4h	$\frac{1}{1+e^{\frac{(V_m+39.57)}{3.68}}}$	$\frac{e^{(0.6*0.8*(V_m+16))}}{0.2(0.000001+e^{(0.6(V_m+16))})}+5$
I_{kt2}	m^2h	$\frac{1}{1+e^{\frac{(V_m+40.3)}{12.3}}}$	$\frac{e^{(0.695*0.966*(V_m+16))}}{0.00818(5.945x10^{-8}+e^{(0.695(V_m-21.04))})}+115.9$

Table 3

Passive and active parameters related to JGC single compartment model

Parameter	Value
L	43μm
Diam	43μm
R_a	35.4 ohm*cm
R_m	111 MΩ
C_m	1μF/cm^2
G_{pas}	1.55×10^{-4} S/cm^2
E_{pas}	−63.5mV
I_{na} density	100 pS/μm^2
I_{cat1} density	0.0025 S/cm^2
I_{cat2} density	0.003 S/cm^2
I_{kt1} density	0.00375 S/cm^2
I_{kt2} density	0.00074 S/cm^2
I_{kt3} density	14 pS/μm^2